Efficient Frequency Conversion in a Degenerate $\chi^{(2)}$ Microresonator

Jia-Qi Wang,[1,2,†] Yuan-Hao Yang,[1,2,†] Ming Li,[1,2] Xin-Xin Hu,[1,2] Joshua B. Surya,[3] Xin-Biao Xu,[1,2] Chun-Hua Dong,[1,2] Guang-Can Guo,[1,2] Hong X. Tang,[3] and Chang-Ling Zou[1,2,*]

[1]*Key Laboratory of Quantum Information, Chinese Academy of Sciences, University of Science and Technology of China, Hefei 230026, People's Republic of China*

[2]*CAS Center For Excellence in Quantum Information and Quantum Physics, University of Science and Technology of China, Hefei, Anhui 230026, People's Republic of China*

[3]*Department of Electrical Engineering, Yale University, New Haven, Connecticut 06511, USA*

(Received 20 November 2020; accepted 25 February 2021; published 29 March 2021)

Microresonators on a photonic chip could enhance nonlinear optics effects and thus are promising for realizing scalable high-efficiency frequency conversion devices. However, fulfilling phase matching conditions among multiple wavelengths remains a significant challenge. Here, we present a feasible scheme for degenerate sum-frequency conversion that only requires the two-mode phase matching condition. When the drive and the signal are both near resonance to the same telecom mode, an on-chip photon-number conversion efficiency up to 42% is achieved, showing a broad tuning bandwidth over 250 GHz. Furthermore, cascaded Pockels and Kerr nonlinear optical effects are observed, enabling the parametric amplification of the optical signal to distinct wavelengths in a single device. The scheme demonstrated in this Letter provides an alternative approach to realizing high-efficiency frequency conversion and is promising for future studies on communications, atom clocks, sensing, and imaging.

DOI: 10.1103/PhysRevLett.126.133601

Introduction.—Coherent frequency conversion processes between distinct frequency bands are necessary for a number of classical and quantum optical applications [1–4], e.g., communication, detection, sensing, and imaging [5–8]. For these applications, we wish to convert the frequencies of the encoded carriers while leaving the information essentially unperturbed. Nonlinear optical processes achieve this goal by compensating for the energy differences between the carriers while also conserving the encoded information [9]. In the past decades, such coherent frequency conversion processes have been experimentally verified [10–13] and have been applied in a wide range of devices, including up-converted single photon detectors [14,15], long-distance entanglement distribution [16,17], and microwave-to-optical transducers [18–22].

Recently, with the improvement of nanofabrication technology, integrated nonlinear photonic chips have made significant technological advances [23–27] and shown better performances than macroscopic waveguides and resonators because of the strong confinement of optical fields and the long lifetime of the optical resonances, which allow high conversion efficiency, excellent scalability, and the potential to integrate with other on-chip components. For example, high-efficiency frequency conversion and strong coupling between optical modes in distinct wavelengths have recently been realized by microring resonators [28–31]. Additionally, materials with strong nonlinearity [$\chi^{(2)}$], such as $LiNbO_3$, AlN, GaAs, and AlGaAs [32–38], have transitioned on chip for achieving even larger photon-photon interaction and other promising qubit-free optical applications [39–41]. Along with the advantages of stability and scalability, the photonic chip also holds great potential for future quantum applications [42,43]. The main challenge for resonant-enhanced coherent frequency conversion is the constraints of simultaneously satisfying energy and momentum conservation for multiple modes at distinct wavelengths, especially for matching the target transitions of atoms or other emitters.

In this Letter, we propose a novel method of achieving resonant-enhanced optical frequency conversion on a photonic chip via a degenerate sum-frequency process using a single input mode. Since both drive and signal are at near resonance with the same telecom mode, only the two-mode phase matching condition is required in this conversion, which is flexible for experiments. Through this scheme, a high photon-number conversion efficiency of 42% is realized, with an FWHM bandwidth of the tuning range over 250 GHz. Furthermore, in the high-power regime, we reveal the cross-band frequency conversion and amplification in a single microresonator, which manifest the advantages of on-chip nonlinear photonic devices in fundamental research and potential applications.

Principle.—Within a microring resonator composed of materials with $\chi^{(2)}$ nonlinearity, there are many modes in the visible and IR frequency bands [33,44]. In general, the nonlinear coupling between the modes due to the $\chi^{(2)}$ nonlinearity can be described by the interaction Hamiltonian [25,44]

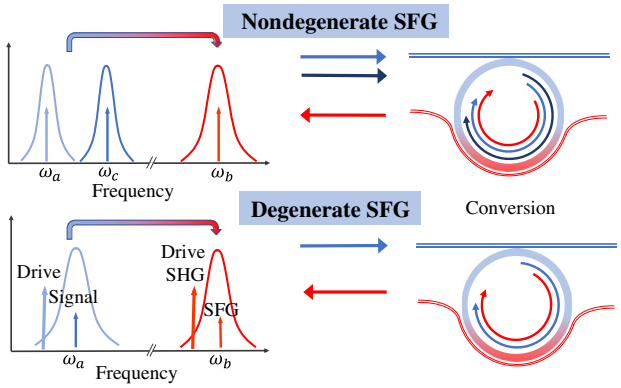

FIG. 1. Schematic illustration of the frequency conversion via nondegenerate sum-frequency generation and degenerate sum-frequency generation models. Comparing the two schemes, the degenerate case only requires the phase matching condition between two modes and produces a second-harmonic generation signal of the drive that nears resonance with the signal mode.

$$H_{\chi^{(2)}} = \sum_{j,k,l} g_{jkl}(a_j a_k b_l^\dagger + \text{H.c.}), \tag{1}$$

where a_j, b_k denote the bosonic operators of the optical modes, with subscripts $j, k \in \mathbb{Z}$ as the mode orbit angular momentum, and g_{jkl} represents the coupling strength. According to the momentum conservation [28], g_{jkl} is nontrivial only for $j + k = l$. For the telecom and visible frequency ranges we are interested in, the mode profiles are similar—thus, $g_{jk(j+k)}$ is approximated by a constant g in the following. For the nondegenerate sum-frequency generation (SFG), as shown in Fig. 1, we drive one IR mode with an intracavity amplitude α_j. Next, we realize the frequency conversion by the linearized Hamiltonian [9] $H_{\text{FC}} = \sum_k (G_j a_k b_{j+k}^\dagger + G_j^* a_k^\dagger b_{j+k})$, which induces coherent coupling between a_k and b_l of distinct wavelengths, while $G_j = 2g_2\alpha_j$ is the stimulated coupling strength. However, the nondegenerate SFG requires a triply resonant condition ($\omega_{a_j} + \omega_{a_k} \approx \omega_{b_{j+k}}$) for energy conservation. In practical applications for converting the telecom photons to match the frequency of narrow atomic transition at ω_{b_l}, the stringent triply resonant condition imposes significant challenges for finding modes that satisfy all requirements.

Instead of demanding matching conditions for nondegenerate modes in SFG, its degenerate counterpart, known as second-harmonic generation (SHG), relaxes the requirements on phase matching and energy matching ($2j = l$ and $2\omega_{a_j} \approx \omega_{b_l}$) because fewer optical modes participate in the interaction. However, SHG is not a linear process, so the conversion is only efficient when the signal power is high enough. Therefore, we propose to drive the mode a_j near resonance and couple the on-resonance signal to the same mode, thus realizing the degenerate SFG (Fig. 1) with the Hamiltonian as

$$H_{\text{FC}} = \sum_j (G a_j b_{2j}^\dagger + G^* a_j^\dagger b_{2j}), \tag{2}$$

which indicates a linear signal conversion process.

Experimental setup.—To demonstrate the frequency conversion by the new scheme, we carried out experiments by an AlN photonic chip [44–47] with the experimental setup shown in Fig. 2(a). Our device uses a 570-nm-wide bus waveguide to couple light into the microrings with a waveguide width of 1.15–1.25 μm, designed for optimal SHG. The radius of our microrings is 30 μm and the mode quality factor at 1560 nm (780 nm) is $1.38 \times 10^6 (8.74 \times 10^5)$ [46,48]. In our experimental setup, a telecom laser is amplified by an erbium-doped fiber amplifier and divided into two beams for drive and signal, respectively. The signal is generated from the laser through an acoustic-optical modulator (AOM, ~100 MHz) with the frequency shifted from the drive laser and is collected by a fiber since the sideband of the AOM is deflected from the input. Then, both drive and signal light are combined through a beam splitter and seeded to the AlN chip through a fiber lens. The converted signal and the generated SHG light (around 780 nm), as well as transmitted drive (around 1560 nm), are collected by fiber lens on the output end of the chip, separated by a wavelength division multiplexer (WDM), and finally collected by photodetectors.

To validate the frequency conversion via degenerate SFG, we send both drive and signal to the selected mode and measure the converted signal via a scanning Fabry-Pérot interferometer at visible wavelength. As shown in Fig. 2(b), on the background of a strong SHG peak due to the drive, there is a small peak of about 100 MHz detuned, corresponding to 22.4 mW and 0.096 mW for the calibrated on-chip power of drive and signal, respectively. Furthermore, to confirm that the weak peak is caused by the SFG rather than other effects, we explore the relationship between the power of the weak peak (P_{Vis}) at visible frequency and the power of the input IR signal (P_{IR}). The experimental results in Fig. 2(c) are well fitted by a linear function $P_{\text{Vis}} = 0.346\, P_{\text{IR}} - 7.9 \times 10^{-4}$ mW in contrast to the P_{IR}^2 scaling for SHG, in which the slope 0.346 is the power efficiency and the negligible residual due to the noise of detector and strong SHG background. The linear relationship confirms the single-mode frequency conversion mechanism.

Precise frequency tuning.—In a microring resonator, the small mode volume is beneficial for nonlinear optical frequency conversion, while it also leads to sparse resonances that impose challenges in practical applications: the resonant frequency determined by cavity geometry is usually different from the wavelength we need, i.e., the target wavelength cannot match the frequency window (FW) of the device for high-efficiency conversion. Therefore, for a useful interface that connects different wavebands, the precise tuning of FW is demanded. The temperature

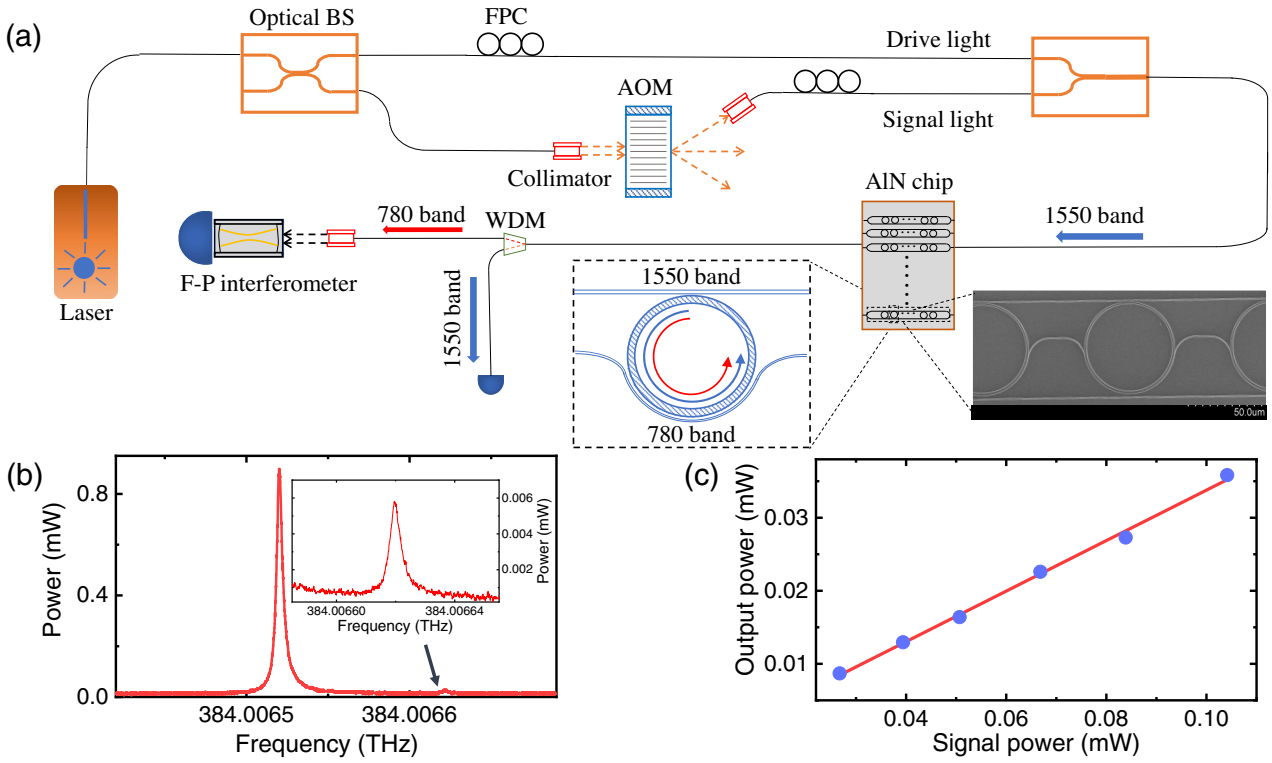

FIG. 2. (a) Experimental setup. Optical BS, optical beam splitter; FPC, fiber polarization controller; AOM, acoustic-optical modulator; WDM, wave division multiplexing. Insert: schematic and SEM picture of our device. (b) Visible output spectra for degenerate SFG. The strong peak represents the SHG of drive light, and the right small peak corresponds to the converted signal. Inset: the converted signal probed by the detector with high gain. (c) The relationship between input and output signal on-chip powers. The blue dots are experimental values, and the red line is a linear fit.

dependence of the mode resonant wavelength offers a convenient way to resolve this problem. Because of the different mode dispersion at the visible (ω_b) and telecom (ω_a) bands, the resonant frequencies of two modes will shift at different rates when changing the device temperature, with the expression $\omega_{a(b)}(T_{\mathrm{ring}}) = \omega_{a(b)}(T_e) + K_{a(b)}(T_{\mathrm{ring}} - T_e)$. Here, $K_{a(b)}$ is the thermal drift coefficient of mode $a(b)$, T_{ring} is the effective temperature of the microresonator, and T_e is the environment temperature of the chip that could be adjusted by a heater in our experiment, as shown in Fig. 3(a). The relative temperature difference $\delta T = T_{\mathrm{ring}} - T_e \simeq c_a|\alpha|^2$ is induced by the optothermal effect in which α represents the intracavity photon amplitude and c_a is the temperature coefficient of mode a [49,50]. As a result, there are two approaches to regulate FW: coarse tuning by changing T_e and keeping δT constant, or fine tuning by the drive light to change δT and the output frequency directly. So, in experiments, we fixed the drive power as a constant and regulated the SFG frequency by changing T_e and the intracavity drive light to characterize the FW tuning ability.

As shown in Fig. 3(b), the SFG signals are generated at different frequencies within about one cavity linewidth FW by varying T_e while keeping the drive near resonance. As expected, the central frequency of the FW decreases with the increasing temperature, with a tuning range of FW over 150 GHz, by changing T_e from 25 °C to 65 °C. We note that the conversion efficiency also changes with temperature, but the peak conversion efficiency persists in this large frequency tuning range. Because of the large chip volume, the precise tuning of the T_e is a challenge, and the thermal response of the whole system is very slow. Therefore, we adopt the other approach for fine tuning the SFG signal frequency. As shown in Fig. 3(c), by changing the drive laser wavelength, the temperature difference δT could be adjusted precisely by the thermal effects of the microring resonator. Here, the intracavity drive power reduces with detuning. Consequently, the FW shows a blueshift as the δT reduces and the efficiency also reduces. Comparing these two methods, the first approach allows a large dynamic range of frequency tuning, while the other approach is suitable for quick and precise controlling.

In our device, the thermal coefficients K_a and K_b determine how fast the resonant frequencies shift with temperature, and their difference $\delta K = K_a - K_b$ determines the sensitivity of phase matching to temperature. To simulate the full frequency conversion bandwidth, we measure the highest frequency conversion efficiency at 30 mW and also fit the thermal coefficients as $K_a = -1.8 \times 10^9$ Hz/K and $K_b = -3.53 \times 10^9$ Hz/K. As shown in Fig. 3(d), the green dot represents the highest SFG

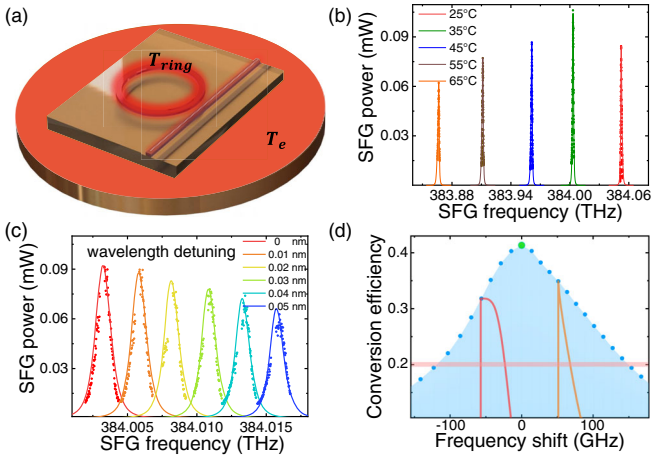

FIG. 3. Frequency tuning. (a) The schematic of the temperature controlling for the on-chip microring resonators. The environment temperature (T_e) could be controlled by a heater, and the device temperature (T_{ring}) could also be adjusted by drive laser. (b) The coarse tuning of frequency conversion by T_e, with on-chip input drive and signal powers of about 23 mW and 0.28 mW, respectively. (c) Fine tuning via T_{ring} by changing the drive wavelength. In both (b) and (c), the dots are the experimental data, and the lines are the calculated results based on device parameters. (d) The prediction of SFG frequency conversion efficiency for different T_e and drive detuning. The zero frequency detuning corresponding to the optimal conversion (∼40%), and the input on-chip drive power is 30 mW. The pink line presents 20% efficiency, which indicates an FWHM of 257 GHz. The red and yellow lines represent the typical results for fine tuning under different T_e (16 K and −16 K away from optimal temperature, respectively).

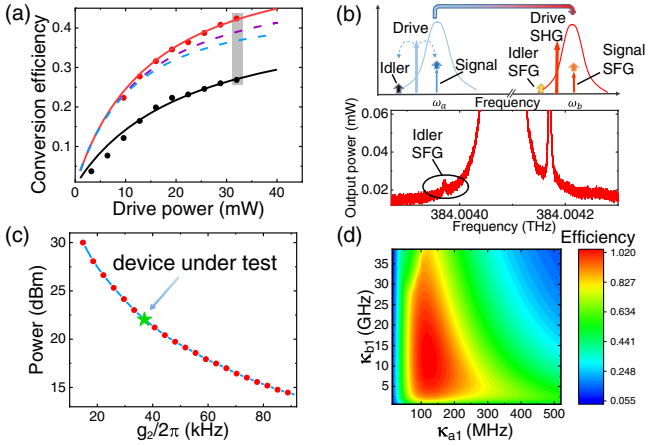

FIG. 4. Cascaded nonlinear effect in frequency conversion. (a) The conversion efficiency of SHG and SFG. The dots are experimental data, and the lines are theoretical predictions. The black line represents the SHG efficiency, the blue dash line is based on the SFG model without cascaded nonlinear effect modification, the purple dash line represents the prediction by including the $\chi^{(2)}-\chi^{(2)}$ processes, and the red solid line represents the theoretical results for the full model that includes both $\chi^{(2)}-\chi^{(2)}$ and intrinsic $\chi^{(3)}$ effects. (b) Our nonlinear process model with cascaded effect and the detailed transmission spectrum at infrared band for degenerate SFG with drive power of 32 mW, which corresponds to the shadow region in (a). The small arrows represent the gain via the cascaded process. (c) The prediction of the required drive power for achieving 100% conversion efficiency for different g_2, with $g_3 \propto g_2^2$ correspondingly and all other parameters are from the actual device. (d) The parameter dependence between the conversion efficiency and the external coupling rates κ_{a1}, κ_{b1}, with all other parameters from the actual device. The drive power is 50 mW.

efficiency, and we set its frequency shift as zero. The shadow predicts the conversion efficiency we can achieve by changing T_e and shows an FWHM of 257 GHz. At each T_e, the conversion FW and efficiency could be adjusted by tuning the drive frequency, as shown by the yellow and red lines in Fig. 3(d). Here, because of the thermal bistability effect [49], the fine tuning shows a sudden jump of efficiency when the system achieves the highest efficiency, and the fine tuning bandwidth varies with the temperature T_e.

Cascaded $\chi^{(2)}$ and $\chi^{(3)}$ in frequency conversion.—According to the physics presented in Fig. 1, the efficiency of the frequency conversion could be enhanced by the drive laser. In Fig. 4(a), we tested the on-chip conversion efficiency against the drive power at optimal working condition. The black and red dots represent the SHG and SFG conversion efficiencies, both of which increase with the drive power and show saturation effects when the drive power (P_d) exceeds 20 mW. However, when fitting the experimental results, the SHG agrees with our theoretical prediction (black curve), while the SFG cannot be fitted (blue curve). It is surprising that the best achieved conversion efficiency, 42%, is about 15% higher than the prediction (blue curve), which indicates an unexpected physical process that amplified the signal.

These experimental results could be explained by the cascaded $\chi^{(2)}$ and $\chi^{(3)}$ effects that indicate the possible multiple nonlinear optics process in a single microresonator. In the microresonator, not only is the $\chi^{(2)}$ enhanced for the SHG and down-conversion processes [28,44,45], but also the $\chi^{(3)}$ is enhanced within the same optical mode. Therefore, for the drive and signal in the IR mode, two processes contribute to the parametric amplification of signal: (i) The degenerate four-wave mixing due to the intrinsic $\chi^{(3)}$ effect, and (ii) the $\chi^{(2)}-\chi^{(2)}$ processes caused by cascaded SHG and the down conversion, which induce an effective $\chi^{(3)}$ process that cannot be neglected when the conversion efficiency is high [51]. So, there is a modification of the Hamiltonian to degenerate SFG as

$$H_{\mathrm{Cascade}} = (G_a a^{\dagger 2} + G_a^* a^2) + H_{\mathrm{FC}}, \tag{3}$$

where $G_a = g_2\beta + 2g_3\alpha^2$, and g_3 is the vacuum coupling strength for the self-Kerr effect [52]. The $g_2\beta$ corresponds

to the $\chi^{(2)}-\chi^{(2)}$ effect, i.e., the effective $\chi^{(3)}$ process, with β being the SHG field of the drive laser. $2g_3\alpha^2$ represents the intrinsic $\chi^{(3)}$ effect. For the IR mode, the two $\chi^{(3)}$ processes are stimulated by the drive, amplify the signal, and generate idle light simultaneously, as schematically illustrated in Fig. 4(b). Therefore, the cascaded effect of the $\chi^{(3)}$ processes and the degenerate SFG would induce an amplification of signal in SHG mode when realizing the frequency conversion, and the amplification is non-negligible for high drive power [$G_a/G_b=\mathcal{O}(1)$]. By including these cascaded nonlinear effects, the experimental results are explained well by the red curve in Fig. 4(a). To further verify the cascaded nonlinear optical processes, we measured the output spectrum using the Fabry-Pérot interferometer with $P_d=38$ mW. As expected, we find an additional idle peak on the left side of the drive SHG light, with the frequency being symmetric with the SFG signal, as shown in the black circle in Fig. 4(b). This weak low-frequency peak corresponds to the idler SFG. Here, the on-chip drive power and conversion efficiency of Fig. 4(b) correspond to the shadow part of Fig. 4(a).

Because of the power limitation in our setup, the amplification effect is not strong enough and only generates a relatively small peak. To further explore the influence of the cascaded nonlinear effect in our experiment, we simulate the parameter dependence of conversion efficiency. As shown in Fig. 4(c), we scale $g_2\propto 1/\sqrt{R}$ and $g_3\propto 1/R$, with the R representing the radius of the microring [54], to study their relationship with conversion efficiency. With the $g_{2,3}$ increasing, the power required to achieve 100% conversion efficiency decreases rapidly. The green pentacle in Fig. 4(c) indicates the parameters of our actual device. Although the coherent coupling between optical modes could be enhanced via increasing the $g_{2,3}$ or the drive power, so that the strong coupling in which the stimulated coupling strength (G_a) exceeds the cavity linewidth (κ_a) could be experimentally achieved [28,30,55], greedily pursuing stronger coupling is not beneficial for the frequency conversion. Thus, we studied the dependence of conversion efficiency on the external coupling rates κ_{a1},κ_{b1}, while keeping the intrinsic loss rate κ_{a0},κ_{b0} fixed, because the intrinsic loss rates are mainly determined by the material itself and the fabrication technique, while the external coupling rates could be adjusted by changing the device geometry. The results are plotted in Fig. 4(d), which show that the highest conversion efficiency is over 100%. These results indicate that by optimizing external coupling rates and intrinsic nonlinear coupling strengths, we can realize a highly efficient frequency conversion for cross-band signal amplification.

Conclusion.—A highly efficient frequency conversion was achieved via a degenerate sum-frequency process, with a maximum conversion efficiency up to 42% and a frequency tuning bandwidth over 250 GHz for efficiency exceeding 20%. The demonstrated degenerate SFG scheme is feasible for a wide range of devices and materials and thus allows the realization of highly efficient frequency conversions for future quantum communications, atom clocks, and sensing applications. Further, we demonstrate the cascaded nonlinear effect and the induced amplification of the converted signal in the same microring resonator, which reveals the advantage of integrated chips in frequency conversion and deserves further investigation.

This work was funded by the National Key Research and Development Program (Grant No. 2016YFA0301300), the National Natural Science Foundation of China (Grants No. 11874342, No. 11934012, No. 11904316, No. 11947234, and No. 11922411), and the Anhui Initiative in Quantum Information Technologies (AHY130200). C. L. Z. was also supported by the Fundamental Research Funds for the Central Universities and the State Key Laboratory of Advanced Optical Communication Systems and Networks, Shanghai Jiao Tong University, China. This work was partially carried out at the USTC Center for Micro and Nanoscale Research and Fabrication.

*Corresponding author.
clzou321@ustc.edu.cn
†J.-Q. W. and Y.-H. Y. contributed equally to this work.

[1] R. W. Boyd, *Nonlinear Optics* (Elsevier, New York, 2003).
[2] M. M. Fejer, Nonlinear optical frequency conversion, Phys. Today **47**, No. 5, 25 (1994).
[3] L. Caspani, D. Duchesne, K. Dolgaleva, S. J. Wagner, M. Ferrera, L. Razzari, A. Pasquazi, M. Peccianti, D. J. Moss, J. S. Aitchison, and R. Morandotti, Optical frequency conversion in integrated devices [Invited], J. Opt. Soc. Am. B **28**, A67 (2011).
[4] R. Arun Kumar, Borate crystals for nonlinear optical and laser applications: A review, J. Chem. **2013**, 154862 (2013).
[5] N. Curtz, R. Thew, C. Simon, N. Gisin, and H. Zbinden, Coherent frequency-down-conversion interface for quantum repeaters, Opt. Express **18**, 22099 (2010).
[6] D. Gottesman, T. Jennewein, and S. Croke, Longer-Baseline Telescopes Using Quantum Repeaters, Phys. Rev. Lett. **109**, 070503 (2012).
[7] L. Li, C.-L. Zou, V. V. Albert, S. Muralidharan, S. M. Girvin, and L. Jiang, Cat Codes with Optimal Decoherence Suppression for a Lossy Bosonic Channel, Phys. Rev. Lett. **119**, 030502 (2017).
[8] X. Guo, C. R. Breum, J. Borregaard, S. Izumi, M. V. Larsen, T. Gehring, M. Christandl, J. S. Neergaard-Nielsen, and U. L. Andersen, Distributed quantum sensing in a continuous-variable entangled network, Nat. Phys. **16**, 281 (2020).
[9] P. Kumar, Quantum frequency conversion, Opt. Lett. **15**, 1476 (1990).
[10] J. Huang and P. Kumar, Observation of Quantum Frequency Conversion, Phys. Rev. Lett. **68**, 2153 (1992).
[11] H. J. McGuinness, M. G. Raymer, C. J. McKinstrie, and S. Radic, Quantum Frequency Translation of Single-Photon

States in a Photonic Crystal Fiber, Phys. Rev. Lett. **105**, 093604 (2010).
[12] S. Clemmen, A. Farsi, S. Ramelow, and A. L. Gaeta, Ramsey Interference with Single Photons, Phys. Rev. Lett. **117**, 223601 (2016).
[13] H. Rütz, K.-H. Luo, H. Suche, and C. Silberhorn, Quantum Frequency Conversion between Infrared and Ultraviolet, Phys. Rev. Applied **7**, 024021 (2017).
[14] A. P. Vandevender and P. G. Kwiat, High efficiency single photon detection via frequency up-conversion, J. Mod. Opt. **51**, 1433 (2004).
[15] A. Samblowski, C. E. Vollmer, C. Baune, J. Fiurášek, and R. Schnabel, Weak-signal conversion from 1550 to 532 nm with 84% efficiency, Opt. Lett. **39**, 2979 (2014).
[16] N. Maring, P. Farrera, K. Kutluer, M. Mazzera, G. Heinze, and H. de Riedmatten, Photonic quantum state transfer between a cold atomic gas and a crystal, Nature (London) **551**, 485 (2017).
[17] Y. Yu, F. Ma, X.-Y. Luo, B. Jing, P.-F. Sun, R.-Z. Fang, C.-W. Yang, H. Liu, M.-Y. Zheng, X.-P. Xie, W.-J. Zhang, L.-X. You, Z. Wang, T.-Y. Chen, Q. Zhang, X.-H. Bao, and J.-W. Pan, Entanglement of two quantum memories via fibres over dozens of kilometres, Nature (London) **578**, 240 (2020).
[18] R. W. Andrews, R. W. Peterson, T. P. Purdy, K. Cicak, R. W. Simmonds, C. A. Regal, and K. W. Lehnert, Bidirectional and efficient conversion between microwave and optical light, Nat. Phys. **10**, 321 (2014).
[19] L. A. Williamson, Y.-H. Chen, and J. J. Longdell, Magneto-Optic Modulator with Unit Quantum Efficiency, Phys. Rev. Lett. **113**, 203601 (2014).
[20] L. Fan, C.-L. Zou, R. Cheng, X. Guo, X. Han, Z. Gong, S. Wang, and H. X. Tang, Superconducting cavity electro-optics: A platform for coherent photon conversion between superconducting and photonic circuits, Sci. Adv. **4**, eaar4994 (2018).
[21] X. Han, W. Fu, C. Zhong, C.-L. Zou, Y. Xu, A. A. Sayem, M. Xu, S. Wang, R. Cheng, L. Jiang, and H. X. Tang, Cavity piezo-mechanics for superconducting-nanophotonic quantum interface, Nat. Commun. **11**, 3237 (2020).
[22] A. Rueda, F. Sedlmeir, M. C. Collodo, U. Vogl, B. Stiller, G. Schunk, D. V. Strekalov, C. Marquardt, J. M. Fink, O. Painter, G. Leuchs, and H. G. L. Schwefel, Efficient microwave to optical photon conversion: an electro-optical realization, Optica **3**, 597 (2016).
[23] Y.-Z. Sun, Y.-P. Huang, and P. Kumar, Photonic Nonlinearities via Quantum Zeno Blockade, Phys. Rev. Lett. **110**, 223901 (2013).
[24] D. V. Strekalov, C. Marquardt, A. B. Matsko, H. G. L. Schwefel, and G. Leuchs, Nonlinear and quantum optics with whispering gallery resonators, J. Opt. **18**, 123002 (2016).
[25] I. Breunig, Three-wave mixing in whispering gallery resonators, Laser Photonics Rev. **10**, 569 (2016).
[26] Y. Li, X. Jiang, G. Zhao, and L. Yang, Whispering gallery mode microresonator for nonlinear optics, arXiv:1809.04878.
[27] J. Xie, J.-Q. Wang, Z.-B. Wang, X.-X. Hu, X. Guo, R. Niu, J. B. Surya, J.-Z. Zhang, C.-H. Dong, G.-C. Guo, H. X. Tang, and C.-L. Zou, Infrared laser locking to a rubidium saturated absorption spectrum via a photonic chip frequency doubler, Opt. Lett. **44**, 1150 (2019).
[28] X. Guo, C. L. Zou, H. Jung, and H. X. Tang, On-Chip Strong Coupling and Efficient Frequency Conversion between Telecom and Visible Optical Modes, Phys. Rev. Lett. **117**, 123902 (2016).
[29] Q. Li, M. Davanço, and K. Srinivasan, Efficient and low-noise single-photon-level frequency conversion interfaces using silicon nanophotonics, Nat. Photonics **10**, 406 (2016).
[30] S. Ramelow, A. Farsi, Z. Vernon, S. Clemmen, X. Ji, J. E. Sipe, M. Liscidini, M. Lipson, and A. L. Gaeta, Strong Nonlinear Coupling in a Si_3N_4 Ring Resonator, Phys. Rev. Lett. **122**, 153906 (2019).
[31] X. Lu, G. Moille, Q. Li, D. A. Westly, A. Singh, A. Rao, S.-P. Yu, T. C. Briles, S. B. Papp, and K. Srinivasan, Efficient telecom-to-visible spectral translation through ultralow power nonlinear nanophotonics, Nat. Photonics **13**, 593 (2019).
[32] J. Lu, J. B. Surya, X. Liu, A. W. Bruch, Z. Gong, Y. Xu, and H. X. Tang, Periodically poled thin-film lithium niobate microring resonators with a second-harmonic generation efficiency of 250,000%/W, Optica **6**, 1455 (2019).
[33] J.-Y. Chen, Z.-H. Ma, Y. M. Sua, Z. Li, C. Tang, and Y.-P. Huang, Ultra-efficient frequency conversion in quasi-phase-matched lithium niobate microrings, Optica **6**, 1244 (2019).
[34] J. Lu, M. Li, C.-L. Zou, A. A. Sayem, and H. X. Tang, Towards 1% single photon nonlinearity with periodically-poled lithium niobate microring resonators, Optica **7**, 1654 (2020).
[35] P. S. Kuo, J. Bravo-Abad, and G. S. Solomon, Second-harmonic generation using $\bar{4}$-quasi-phasematching in a GaAs whispering-gallery-mode microcavity, Nat. Commun. **5**, 3109 (2014).
[36] L. Chang, A. Boes, X. Guo, D. T. Spencer, M. J. Kennedy, J. D. Peters, N. Volet, J. Chiles, A. Kowligy, N. Nader, D. D. Hickstein, E. J. Stanton, S. A. Diddams, S. B. Papp, and J. E. Bowers, Heterogeneously integrated GaAs waveguides on insulator for efficient frequency conversion, Laser Photonics Rev. **12**, 1800149 (2018).
[37] E. J. Stanton, J. Chiles, N. Nader, G. Moody, N. Volet, L. Chang, J. E. Bowers, S. Woo Nam, and R. P. Mirin, Efficient second harmonic generation in nanophotonic GaAs-on-insulator waveguides, Opt. Express **28**, 9521 (2020).
[38] L. Chang, A. Boes, P. Pintus, J. D. Peters, M. Kennedy, X.-W. Guo, N. Volet, S.-P. Yu, S. B. Papp, and J. E. Bowers, Strong frequency conversion in heterogeneously integrated GaAs resonators, APL Photonics **4**, 036103 (2019).
[39] M. Li, Y.-L. Zhang, H. X. Tang, C.-H. Dong, G.-C. Guo, and C.-L. Zou, Photon-photon quantum phase gate in a photonic molecule with $\chi^{(2)}$ nonlinearity, Phys. Rev. Applied **13**, 044013 (2020).
[40] M. Heuck, K. Jacobs, and D. R. Englund, Controlled-Phase Gate Using Dynamically Coupled Cavities and Optical Nonlinearities, Phys. Rev. Lett. **124**, 160501 (2020).
[41] S. Krastanov, M. Heuck, J. H. Shapiro, P. Narang, D. R. Englund, and K. Jacobs, Room-temperature photonic logical qubits via second-order nonlinearities, arXiv:2002.07193.
[42] J. Wang, F. Sciarrino, A. Laing, and M. G. Thompson, Integrated photonic quantum technologies, Nat. Photonics **14**, 273 (2020).

[43] A. W. Elshaari, W. Pernice, K. Srinivasan, O. Benson, and V. Zwiller, Hybrid integrated quantum photonic circuits, Nat. Photonics **14**, 285 (2020).

[44] X. Guo, C. Zou, and H. Tang, Second-harmonic generation in aluminum nitride microrings with 2500%/W conversion efficiency, Optica **3**, 1126 (2016).

[45] X. Guo, C.-L. Zou, C. Schuck, H. Jung, R. Cheng, and H. X. Tang, Parametric down-conversion photon-pair source on a nanophotonic chip, Light Sci. Appl. **6**, e16249 (2017).

[46] J. B. Surya, X. Guo, C.-L. Zou, and H. X. Tang, Control of second-harmonic generation in doubly resonant aluminum nitride microrings to address a rubidium two-photon clock transition, Opt. Lett. **43**, 2696 (2018).

[47] A. W. Bruch, X. Liu, J. B. Surya, C.-L. Zou, and H. X. Tang, On-chip $\chi^{(2)}$ microring optical parametric oscillator, Optica **6**, 1361 (2019).

[48] A. W. Bruch, X. Liu, X. Guo, J. B. Surya, Z. Gong, L. Zhang, J. Wang, J. Yan, and H. X. Tang, 17000%/W second-harmonic conversion efficiency in single-crystalline aluminum nitride microresonators, Appl. Phys. Lett. **113**, 131102 (2018).

[49] X.-X. Hu, J.-Q. Wang, Y.-H. Yang, J. B. Surya, Y.-L. Zhang, X.-B. Xu, M. Li, C.-H. Dong, G.-C. Guo, H. X. Tang, and C.-L. Zou, All-optical thermal control for second-harmonic generation in an integrated microcavity, Opt. Express **28**, 11144 (2020).

[50] Y. Feng, Y. Zheng, F. Zhang, J. Yang, T. Qin, and W. Wan, Passive fine-tuning of microcavity whispering gallery mode for nonlinear optics by thermo-optical effect, Appl. Phys. Lett. **114**, 101103 (2019).

[51] M. Li, C.-L. Zou, C.-H. Dong, X.-F. Ren, and D.-X. Dai, Enhancement of second-harmonic generation based on the cascaded second- and third-order nonlinear processes in a multimode optical microcavity, Phys. Rev. A **98**, 013854 (2018).

[52] See the Supplemental Material, which includes Ref. [53], at http://link.aps.org/supplemental/10.1103/PhysRevLett.126.133601 for a detailed derivation.

[53] J. D. Cohen, S. M. Meenehan, G. S. MacCabe, S. Gröblacher, A. H. Safavi-Naeini, F. Marsili, M. D. Shaw, and O. Painter, Phonon counting and intensity interferometry of a nanomechanical resonator, Nature (London) **520**, 522 (2015).

[54] X. Guo, C.-L. Zou, H. Jung, Z. Gong, A. Bruch, L. Jiang, and H. X. Tang, Efficient generation of a near-visible frequency comb via Cherenkov-like radiation from a Kerr microcomb, Phys. Rev. Applied **10**, 014012 (2018).

[55] Y. Zheng, J. Yang, Z. Shen, J. Cao, X. Chen, X. Liang, and W. Wan, Optically induced transparency in a micro-cavity, Light Sci. Appl. **5**, e16072 (2016).